



Stability of different Ni supported catalysts in the in-line steam reforming of biomass fast pyrolysis volatiles

Laura Santamaria, Gartzen Lopez*, Aitor Arregi, Maider Amutio, Maite Artetxe, Javier Bilbao, Martin Olazar

Department of Chemical Engineering, University of the Basque Country UPV/EHU, P.O. Box 644, E48080 Bilbao, Spain

ARTICLE INFO

Keywords:
Hydrogen
Pyrolysis
Reforming
Biomass
Deactivation
Catalyst

ABSTRACT

The performance and stability of different Ni supported catalysts have been studied in a continuous bench scale plant fitted with a conical spouted bed reactor for biomass pyrolysis at 500 °C and a fluidized bed reactor for the in line catalytic steam reforming of pyrolysis volatiles at 600 °C. The metal oxides selected as Ni supports have been Al₂O₃, SiO₂, MgO, TiO₂ and ZrO₂, and all the catalysts have been prepared by the wet impregnation method. Significant differences have been observed in the performance and stability of the catalysts, with the most suitable ones concerning the evolution of bio-oil oxygenate conversion and H₂ yield with time on stream being as follows: Ni/Al₂O₃ > Ni/ZrO₂ > Ni/MgO > Ni/TiO₂ > Ni/SiO₂. The activity and stability are explained based on the properties of the catalysts, which have been measured prior and after their use, by means of different techniques: N₂ adsorption/ desorption, X-ray fluorescence (XRF), X-ray powder diffraction (XRD), temperature programmed oxidation (TPO), in-line monitoring by Fourier-transform infrared spectroscopy-temperature programmed oxidation (FTIR-TPO), scanning electron microscopy (SEM), and transmission electron microscopy (TEM).

1. Introduction

The depletion of fossil fuels and the necessity to attenuate global warming have generated a growing interest in alternative routes for the sustainable production of fuels and raw materials. In this scenario, the routes for biomass thermochemical valorization may cover the growing demand of H₂ for use as fuel, raw material for the production of fertilizers and hydroprocessing of oil fractions [1–5]. These new processes may complement the H₂ production in already installed units for the steam reforming of methane and other fossil fuels.

Amongst the thermochemical methods for the production of hydrogen from biomass, supercritical water gasification, steam gasification and fast pyrolysis followed by steam reforming of the bio-oil produced are noteworthy. Steam gasification has been proven to be a suitable method, since it can generate H₂ rich syngas [4,6,7]. Nevertheless, it faces significant drawbacks, such as the operational problems associated with the tar in the syngas [8–12]. The steam reforming of bio-oil has certain advantages in comparison with the direct biomass gasification, as it requires lower temperatures and so lower energy requirements. However, it requires two independent reaction units (pyrolysis and reforming) and the need for bio-oil condensation and its

transportation to the reforming unit. Moreover, the instability of the bio-oil under storage, along with the difficulties involving its feeding (due to incomplete vaporization) lead to a decrease in H₂ yield [13–15].

An interesting alternative proposed to avoid the aforementioned problems is the direct route of pyrolysis and in line reforming of the volatiles [4,16–21]. This process allows integrating two reactors in the same unit and so performing pyrolysis and reforming steps under optimum conditions, thus operating at lower temperatures than gasification and avoiding tar formation. Given that the volatile stream from the raw biomass pyrolysis is reformed, a higher H₂ production is obtained compared to that of bio-oil reforming, in which a bio-oil fraction polymerizes throughout the vaporization process and leads to a solid residue [22].

The mechanisms of catalyst deactivation occurring during oxygenate reforming are of different nature: chemical (poisoning, coking, phase changes), mechanical (attrition/entrainment) and thermal (sintering) [23,24]. Although the relevance order of these mechanisms depends on the catalyst and reaction conditions, coke formation kinetics are fast due to the unstable nature of bio-oil oxygenates (especially phenolic compounds) [23,25]. Consequently, the fast catalyst deactivation involves the greatest challenge in the design of reforming

* Corresponding author.

E-mail address: gartzen.lopez@ehu.es (G. Lopez).

<https://doi.org/10.1016/j.apcatb.2018.09.081>

Received 12 June 2018; Received in revised form 18 September 2018; Accepted 25 September 2018

Available online 27 September 2018

0926-3373/ © 2018 Elsevier B.V. All rights reserved.

catalysts, which requires the selection of a suitable metal as active phase, a promoter that increases activity and/or stability and a support that facilitates metal dispersion and the diffusion of bulky oxygenates [7].

A wide range of base transition metals (Ni, Co and Fe) and noble metals (Rh, Pt, Ir and Ru) have been studied in the literature for the reforming of oxygenates derived from biomass pyrolysis [17,26,27]. Amongst them, Ni and Rh based catalysts have led to the highest reforming activities [28], but greater attention has been paid to Ni as active phase due to the high cost of the noble metals.

In addition, as is well known in the literature, the support plays a key role in the activity and stability of the catalysts [29]. Generally, Al_2O_3 has been the most widely used support in commercial Ni steam reforming catalysts, as its high specific surface area eases Ni dispersion, and its mechanical strength provides stability to the catalyst [30]. However, the acid properties of this support promote coke deposition under reaction conditions and lead to catalyst deactivation [31,32]. Mesoporous SiO_2 materials are attracting increasing attention due to their high specific surface area, neutral acidity/basicity property and excellent thermal stability [33], which allow attaining high metal dispersion and low coke deposition rates. In addition, it has been reported that metal oxides with basic properties, such as MgO , ZrO_2 , CeO_2 or La_2O_3 delay coke formation [34–36]. Thus, the amphoteric character of ZrO_2 , presenting both acid and basic properties on its surface, conferred redox functions upon this support [30,37]. Moreover, ZrO_2 has high mechanical strength and thermal stability [38,39], and also enhances steam adsorption and activates the gasification of hydrocarbons or the coke precursors adsorbed on the catalyst surface in the steam reforming reactions, thereby enhancing hydrogen yield and coke resistance [40–42].

Another support used in reforming reactions is TiO_2 due to both its potential benefits as a reducible oxide (providing unique electronic interactions with the metal that promote the catalytic activity under milder reaction temperature conditions) and its well-known ability to delay coke formation when its suitable content favours the electronic interaction with the metal [43,44].

A considerable number of studies have been carried out to ascertain the performance of reforming catalysts against deactivation. However, most of them have been conducted by using model compounds, and studies using real raw bio-oil are still limited [4]. In a previous study, the initial activity of $\text{Ni}/\text{Al}_2\text{O}_3$, Ni/SiO_2 , Ni/MgO , Ni/TiO_2 and Ni/ZrO_2 catalysts has been analyzed in the steam reforming of biomass pyrolysis volatiles, and the initial highest activity of $\text{Ni}/\text{Al}_2\text{O}_3$ and Ni/ZrO_2 has been related to the suitable physical properties of the support, which enhance a proper metal dispersion [45]. Apart from the catalyst initial activity, studies involving catalyst stability and its deactivation mechanism are essential for a catalytic process. Consequently, the aim of this research was to analyze the influence the support has on the performance and stability of Ni based catalysts in the in-line reforming of the volatile oxygenate stream formed in the biomass fast pyrolysis. In order to meet this objective, a detailed characterization (N_2 adsorption-desorption, XRD, XRF, TPO, FTIR-TPO, SEM, TEM) of fresh and deactivated catalysts was carried out to determine the origin of the deactivation and so step further in the understanding of the relationship between the catalysts features and their performance.

2. Experimental

2.1. Materials

Pine wood (*pinus insignis*) was selected in this study as the most representative biomass residue in Europe. The sample preparation and main properties (ultimate and proximate analysis, HHV) are reported elsewhere [46]. Particle size between 1–2 mm was chosen in order to guarantee the good performance of the solid feeding system.

The different oxides selected as catalytic supports were Al_2O_3 (Alfa

Aesar), SiO_2 (Merck), MgO (Sigma Aldrich), TiO_2 (Alfa Aesar) and ZrO_2 (Alfa Aesar). An adequate pre-treatment of all supports was carried out to ensure suitable fluidization conditions in the reforming step [19]. Thereby, particles in the 0.4–0.8 mm size range were selected by milling and sieving. The Ni catalysts were prepared by wet impregnation of the support with an aqueous solution of $\text{Ni}(\text{NO}_3)_2 \cdot 6\text{H}_2\text{O}$ (VWR Chemicals, 99%). After this operation, the catalysts were dried at 100 °C for 24 h, followed by calcination at 700 °C for 3 h, but in the case of Ni/MgO the calcination temperature was fixed at 500 °C to improve the reducibility of the catalyst [35]. A nominal content of 10 wt% Ni was selected in all catalysts, as this is the optimum value reported in the literature [47,48].

2.2. Characterization of the fresh and deactivated catalysts

The textural properties of the fresh and deactivated catalysts were characterized by N_2 adsorption-desorption isotherms at 77 K, in a Micromeritics ASAP 2010. Thus, the surface area was calculated by the Brunauer–Emmett–Teller (BET) method and the distribution of the pore volume and pore diameter were obtained by Barret–Joyner–Halenda (BJH) method. The total metal loading (wt%) in each catalyst (9.51–9.79 wt% range, close to the 10 wt% nominal value) were quantified by X-Ray Fluorescence (XRF) spectrometry (WDXRF, PANalytical AXIOS). Temperature Programmed Reduction (TPR) was carried out for determining the reduction temperature of the different metallic phases in each catalyst. These tests were conducted in an AutoChem II 2920 Micromeritics and the results have been reported in detail in a previous paper [45]. X-Ray powder Diffraction (XRD) patterns of the reduced and deactivated catalysts were recorded in a Bruker D8 Advance diffractometer. The Ni particle size was calculated by using the Scherrer formula:

$$d_{\text{MO}} = \frac{k \lambda}{\beta \cos \theta} \quad (1)$$

where d_{MO} is the average crystallite size; k is Scherrer constant, whose overall value is 0.9; λ is the length of the radiation wave (average $k\alpha = 1.541874 \text{ \AA}$); θ is the position of the diffraction peak corresponding to the metal to be analyzed; β is the average width of the diffraction peak of the sample, which should be corrected taking into account the contribution of the measuring equipment (0.08°).

The coke content of the catalysts was determined by Temperature Programmed Oxidation (TPO), in a Thermobalance (TGA Q5000 TA Instruments) coupled to a mass spectrometer (Thermostat Balzers Instrument). The procedure entails the stabilization of the signal with a N_2 stream (50 mL min^{-1}) at 100 °C and subsequent oxidation with air (50 mL min^{-1}) following a ramp of $5^\circ \text{C min}^{-1}$ to 800 °C, with this temperature keeping for 30 min to guarantee total coke combustion. The combined MS/FTIR-TPO analysis of the coke was performed in a Nicolet 6700 (Thermo) using a transmission cell, 60 scans, and a resolution of 4 cm^{-1} , which was connected online with a mass spectrometer (OMNI STAR TM) to analyze the signal of CO_2 produced during the TPO. The samples of deactivated catalysts (10 mg) were pelletized with KBr (150 mg, purity > 99%). The sample was treated under vacuum at 100 °C to desorb water and remove impurities. When temperature was stable at 100 °C, an air flow (60 mL min^{-1}) was introduced into the combustion chamber at the same time as temperature was increased to 550 °C following a ramp of $5^\circ \text{C min}^{-1}$, and this temperature was kept for 60 min.

The Scanning Electron Microscopy (SEM) of the deactivated catalysts was carried out in a JEOL JSM-6400 apparatus, with a W filament. The acceleration voltage applied to the electron beam was 20 kV and the intensity was between $6 \cdot 10^{-11}$ and $6 \cdot 10^{-10} \text{ A}$. The studied solids were prepared in the form of tablets and they have been adhered to a bronze support with colloidal Ag paste, for the subsequent application of the technique described above. The nanometer level images of the catalysts were obtained using a Transmission Electron Microscope (TEM) (Phillips CM200) with a supertwin lens (punctual resolution of 0.235 nm), fitted

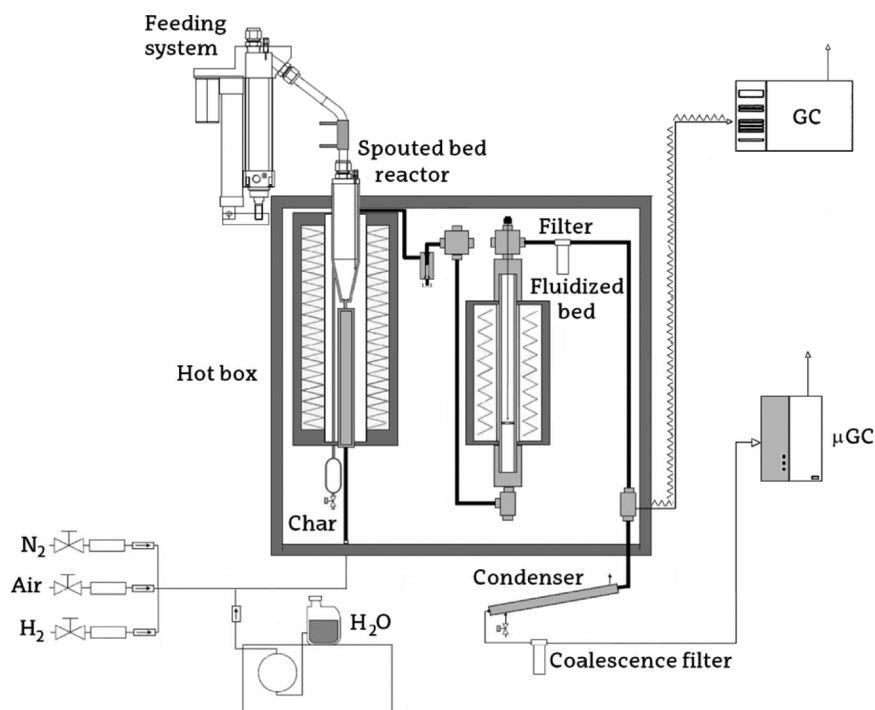


Fig. 1. Diagrammatic representation of the bench scale plant for continuous pyrolysis-reforming of biomass.

with an EDX microanalysis system (Energy-Dispersive X-ray spectroscopy), with the resolution being 137.4 eV. The samples were placed in a double inclination sample holder (Philips PW6595/05), where vacuum was generated and the images were obtained.

2.3. Reaction equipment

The experimental reaction system consists of a bench scale plant, whose scheme is shown in Fig. 1. The good performance of the experimental two-step system has been proven in previous studies [19,46,49]. The unit is provided with two reactors in-line: a conical spouted bed reactor (CSBR) in which the biomass pyrolysis was carried out, and a fluidized bed reactor (FBR) for the in-line reforming of pyrolysis volatiles. The CSBR dimensions are as follows: height of the conical section, 73 mm; diameter of the cylindrical section, 60.3 mm; angle of the conical section, 30°; diameter of the bed bottom, 12.5 mm, and diameter of the gas inlet, 7.6 mm. Additionally, a lateral outlet pipe is located above the bed surface for the removal of char particles from the bed, and so attenuate secondary reactions of pyrolysis volatiles. Moreover, a gas preheating section filled with stainless steel pipes is placed below the gas inlet of the reactor in order to increase the surface area for heat transfer. A 1250 W radiant oven heated the pyrolysis reactor, which is provided with two K-type thermocouples located inside the CSBR (one in the bed annulus and the other one close to the wall) in order to control the reaction temperature.

The dimensions of the fluidized bed used are as follows: diameter of 38.1 mm and length of 440 mm. A thermocouple was located inside the catalyst bed for controlling the temperature, and the reactor was placed inside a radiant oven (550 W). A high efficiency cyclone removes the fine char particles entrained from the CSBR, while the volatile stream leaving the FBR circulates through a sintered steel filter (5 μ m) to retain catalyst fines elutriated. The reaction equipment along with all the interconnection pipes, the high-efficiency cyclone, and the filter are located inside an oven kept at 270 °C, which avoids the condensation of steam or pyrolysis products in the elements connecting the reactors.

This CSBR configuration leads to stable spouting regime and ensures flash pyrolysis conditions due to the high heat and mass transfer rates and short residence times of the volatiles in the reactor. Previous

studies have demonstrated a good performance of the CSBR in the pyrolysis of biomass [50,51], plastics [52,53] and tyres [54,55]. It is to note that the FBR operates under isothermal conditions and allows minimising operational problems due to coke deposition, such as bed clogging [56,57]. Moreover, given the fast deactivation rate in the reforming of oxygenated compounds, the FBR is a suitable alternative for scaling up the process, as it allows for catalyst circulation strategies with ex situ regeneration.

The reaction equipment has different systems for the continuous feeding of biomass, water and gases (N_2 , air, H_2), a system for the analysis of the volatile stream and incondensable gases and a condensation system (Fig. 1). The biomass feeding system enables operating in continuous regime and is made up of a cylindrical vessel equipped with a vertical shaft connected to a piston placed below the biomass bed. A vibration system is actuated at the same time as the piston rises, and so the feed is discharged into the reactor through a pipe cooled with tap water. Moreover, in order to avoid the entrance of the volatile stream into the feeding vessel, a small nitrogen flow rate is introduced into the feeder.

A high precision Gilson 307 pump has been used to measure the water flow rate. Water is vaporized prior entering the forced convection oven by means of a heating cartridge located inside the hot box, and is then fed into the pyrolysis reactor. The utilization of steam as fluidizing agent in the pyrolysis reactor instead of an inert gas (as N_2) avoids the dilution of the gaseous stream in the reforming reactor and eases the condensation of the volatile products (non-reacted oxygenates and water). Previous studies have proven that use of steam instead of N_2 in the pyrolysis step has little influence on product distribution [19]. In addition, N_2 , air and H_2 can be fed into the pyrolysis reactor, i.e., N_2 is used as fluidizing agent during the heating process and H_2 to reduce the Ni catalyst prior to the reforming reaction.

The analysis of the volatiles derived from the reforming reactor has been carried out on-line by means of a GC Varian 3900 provided with a HP-Pona column and a flame ionization detector (FID). The sample has been injected into the GC by means of a line thermostated at 280 °C, once the reforming reactor outlet stream has been diluted with an inert gas. A micro GC (Varian 4900) has been used to analyze on-line the non-condensable gases once the outlet stream of the reforming reactor

Table 1
Product distribution obtained in the pyrolysis step (at 500 °C).

Compound	Yield (wt %)
Gas	7.3
CO	3.38
CO ₂	3.27
CH ₄	0.36
Hydrocarbons (C ₂ –C ₄)	0.3
H ₂	0.04
Bio-oil	75.3
Acids	2.73
Aldehydes	1.93
Alcohols	2
Ketones	6.37
Phenols	16.49
Furans	3.32
Saccharides	4.46
Water	25.36
Char	17.3

has been condensed (cooled with tap water) and filtered (coalescence element).

2.4. Experimental conditions

The suitable operating conditions in each reactor were established in previous studies [19,58]. Given the additional complexity of using steam as fluidizing agent in both steps, the spouted and fluidized bed particle sizes were carefully selected in order to achieve an adequate fluidization regime. Thus, 30 g of silica sand with a particle size in the 0.3–0.35 mm range were introduced in the CSBR, while the bed in the FBR was made up of a mixture of reforming catalyst (50 wt%) and inert sand, with the total mass being 25 g. The particle size of the catalyst was in the 0.4–0.8 mm range and that of the inert silica sand in the 0.3–0.35 mm range.

Biomass was pyrolysed at 500 °C in all the runs, as a previous study proved this temperature was the optimum one to maximize bio-oil yield [50]. Similarly, the reforming temperature was fixed at 600 °C, as the runs conducted at higher temperatures (700 °C) hardly improve the experimental results [19] and lead to Ni sintering [59]. It should be noted that, prior to the runs, the catalyst was in situ reduced at 710 °C for 4 h under 10 vol% H₂ stream, which are the conditions established in a previous paper dealing with the study of the activity at zero time on stream of the same catalysts [45].

With the aim of comparing the performance of all the catalysts prepared, the same operating conditions were used in their testing. Thus, a steam/biomass (S/B) ratio of 4 was selected in all the experiments, with a continuous biomass feed rate of 0.75 g min^{−1} and a water feed rate of 3 ml min^{−1}. Likewise, the molar steam/carbon (S/C) ratio in the reforming step was of 7.7. It should be noted that the amount of carbon contained in the char formed in the pyrolysis step was not considered in the calculation of this ratio. Finally, a space time of 20 g_{cat} min g_{volatiles}^{−1} has been used.

In order to ensure steady state conditions, the reformed products were analyzed on-line in the GC and micro GC once several minutes of continuous operation have elapsed. Furthermore, to ensure the reproducibility of the results, the runs have been repeated at least 3 times under the same experimental conditions.

2.5. Reaction indexes

The conversion and the individual product yields have been taken as the key reaction indexes for evaluating the performance of the different catalysts prepared. Reforming conversion has been defined as the ratio between the C equivalent units in the gaseous product and those in the feed of the reforming step:

$$X = \frac{C_{\text{gas}}}{C_{\text{volatiles}}} 100 \quad (2)$$

It should be noted that the C amount contained in the char produced in the pyrolysis step has not been considered in Eq. (1).

The yield of each individual product has been calculated as:

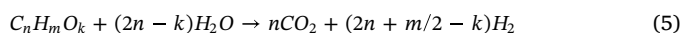
$$Y_i = \frac{F_i}{F_{\text{volatiles}}} 100 \quad (3)$$

where F_i and $F_{\text{volatiles}}$ are the molar flow rates of product i and the pyrolysis volatiles at the inlet of the reforming reactor, respectively, both given in C equivalent units.

The hydrogen yield was defined based on the maximum allowable by stoichiometry:

$$Y_{\text{H}_2} = \frac{F_{\text{H}_2}}{F_{\text{H}_2}^0} 100 \quad (4)$$

where F_{H_2} is the H₂ molar flow rate and $F_{\text{H}_2}^0$ the maximum allowable by the following stoichiometry:



H₂ production has been calculated as the mass of H₂ produced per biomass mass unit fed into the pyrolysis step:

$$P_{\text{H}_2} = \frac{m_{\text{H}_2}}{m_{\text{Biomass}}^0} 100 \quad (6)$$

3. Results

3.1. Pyrolysis products

Table 1 summarizes the product yields obtained in the pyrolysis of biomass, which have been lumped into three fractions: bio-oil, gas and char. More details about the product distribution obtained in the biomass fast pyrolysis in a conical spouted bed reactor have been reported elsewhere [19,50]. As observed, bio-oil was the main product with a yield over 75%, which is evidence of the excellent performance of the CSBR for solid waste fast pyrolysis [60–62]. The bio-oil obtained is made up of a complex mixture of oxygenated compounds (acids, aldehydes, alcohols, ketones, phenols, furans and saccharides), and a significant amount of water due to dehydration reactions and the original moisture content.

The gaseous product stream is formed by mainly CO and CO₂ due to the pyrolysis conditions (relatively low temperatures and short residence times) that minimize secondary cracking reactions. As mentioned above, the char formed was continuously removed through a lateral outlet, thus avoiding its accumulation. This continuous char removal allows minimizing secondary reactions of pyrolysis volatiles on the char surface [63] and maximizing the oxygenate yield, as well as improving the quality of the char for future applications [64].

3.2. Effect of the support on the activity and deactivation of the catalysts

In order to determine the influence the support has on the catalytic performance and stability of the different Ni based catalysts, the evolution of oxygenate conversion (Fig. 2) and product yields (Fig. 3) with time on stream have been studied. The properties of the catalyst used and their role in the reforming step are essential for the interpretation of results. The individual reactions in the reforming step are as follows:

Oxygenate steam reforming:



Water gas shift (WGS) reaction:



Oxygenate cracking (secondary reaction):

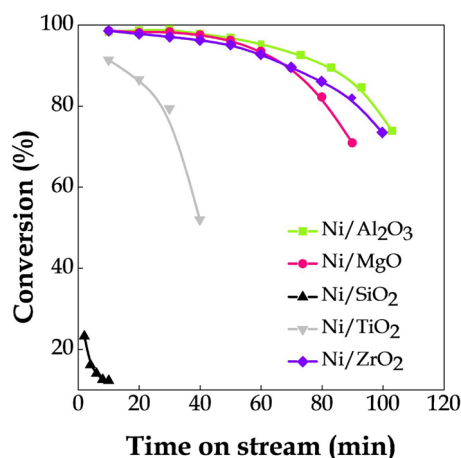
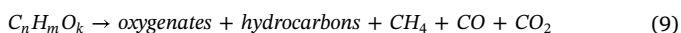


Fig. 2. Effect of the support used for preparing the Ni catalysts on the evolution of oxygenates conversion with time on stream.



Methane (and hydrocarbons) steam reforming:



Table 2 and Table 3 show the values of the textural properties and average Ni particle diameter on the catalyst surface for the fresh and deactivated catalysts. These values have been determined using the techniques and conditions reported in Section 2.2. It is to note that the interpretation of the results should consider the different duration of the experiments, which is due to the different deactivation kinetics observed for the different catalysts (Fig. 2).

Remarkable differences are observed in Fig. 2. Thus, almost complete conversion (> 98%) was attained at zero time on stream for Ni/Al₂O₃, Ni/MgO and Ni/ZrO₂ catalysts, whereas the conversion on the Ni/TiO₂ catalyst was 91% and on the Ni/SiO₂ one was as low as 23%. The higher activity at zero time on stream for the Ni/Al₂O₃ catalyst is related to its properties, with a small average Ni crystallite size (10 nm), a remarkable BET surface area and a high Ni dispersion (10%). The Ni/ZrO₂ catalyst clearly shows poorer textural properties and lower dispersion (4%) than the Ni/Al₂O₃ catalyst. However, the redox capacity of ZrO₂ contributes to improving its activity [37,38].

An explanation for the Ni/MgO catalyst significant activity is based on oxygenate accessibility to the reaction sites. Thus, although MgO has a very low BET surface area (1 m² g⁻¹) and does not favour metal dispersion, Ni is mainly located on the external surface of the support, which improves the accessibility of oxygenates to Ni sites. Basagiannis and Verykios [65] also attributed to MgO the capacity to promote oxygen and/or hydroxyl radical spillover to the Ni sites. On the other hand, SiO₂ is the support with better physical properties and Ni dispersion (9%), but its porous structure (mainly made up of micropores) hindered the access of oxygenate bulky molecules, and therefore a very limited activity was observed. Finally, the Ni/TiO₂ catalyst showed a limited activity that is associated with the poor dispersion attained on this support (2%).

The H₂ production by mass unit of the biomass in the feed (Fig. 3) revealed the pyrolysis-reforming conversion efficiency. Thus, maximum H₂ productions of 10.17, 9.08 and 10.73 wt% for Ni/Al₂O₃, Ni/MgO and Ni/ZrO₂, respectively were obtained at zero time on stream. It is to note that the H₂ molar flow rate obtained with these catalysts is almost (approximately 98%) the thermodynamic equilibrium value. Furthermore, a lower H₂ production was obtained for Ni/SiO₂ and Ni/TiO₂, with values of 1.64 and 7.21 wt%, which are evidence of the unsuitable properties of these supports for the reforming conditions. Besides, comparing the results obtained with that of the thermodynamic equilibrium, Ni/TiO₂ also shows lower activity for WGS reaction than Ni/

Al₂O₃, Ni/MgO and Ni/ZrO₂, with H₂ molar flow rate being 90% of that at thermodynamic equilibrium.

Comparing these results of H₂ production with those by other authors, Waheed et al. [66] reported a maximum H₂ production of 6.1 wt% on a 10 wt% Ni-dolomite catalyst in the pyrolysis/reforming of rice husk. Ye et al. [67] studied size-confined Ni catalysts on acidic MCM-41 supports obtaining a maximum H₂ production of 4.3 wt%.

The deactivation of the catalyst reduces oxygenate conversion with time on stream (Fig. 2) and the yields of the outlet products (Fig. 3). Each pair of graphs in Fig. 3 corresponds to a given catalyst, with the yields of hydrocarbons and methane being plotted in the lower graph of the pair due to their low yield. As observed, H₂ and CO₂ yields decrease with time on stream due to the deactivation of the Ni sites for WGS (Eq. (8)) and reforming (Eqs. (7) and (10)) reactions. However, the yields of hydrocarbons and methane increase with time on stream due to the attenuation of the steam reforming reactions. Oxygenate decomposition reactions (Eq. (9)) take place in parallel to reforming ones and so the attenuation of the latter leads to hydrocarbon and methane formation by cracking reactions. The CO yield remains almost constant or it even reaches a maximum due to a balance among the attenuation of reforming reactions (Eqs. (7) and (10)), increase of its formation by cracking mechanisms (Eq. (9)) and decrease of its conversion by WGS reaction (Eq. (8)). A study on the thermodynamic equilibrium shows that the WGS reaction activity decreases as time on stream is increased, except for Ni/Al₂O₃ catalyst for which H₂ molar flow rate remains close to 98% of that corresponding to equilibrium, even after 103 min. The increase in the deactivation rate with the reaction extent is attributed to the role played by the oxygenate coke precursors, given that their yield increases with time on stream, as observed in Fig. 3.

The results in Figs. 2 and 3 show notable differences in the stability of the studied catalysts. The Ni/Al₂O₃ catalyst showed a stable activity in the first 30 min on stream (presumably due to its high activity and the fact that it is in excess). Carbon conversion then decreased from 98.4 to 73.9% for 100 min on stream (Fig. 2), while the hydrogen yield dropped from 92.4 to 62.6% (Fig. 3a), which is an indication of a notable deactivation of the catalyst. Regarding Ni/MgO catalyst, a reduction in the conversion from 98.5 to 70.9% after 90 min is observed. In the case of Ni/ZrO₂ catalyst (slightly less active) (Fig. 3e), activity decreases from the beginning of the reaction, with carbon conversion dropping from 98.5 to 73.5% and also H₂ yield (from 92.7 to 61.9%) for 100 min on stream. This lower deactivation rate is a consequence of the positive impact of redox and oxygen storage capacity of ZrO₂ to minimize coke deposition [37,38]. A comparison of the product distributions shown in Fig. 3 for the different catalysts reveals that higher CH₄ and HC yields are obtained using Ni/MgO catalysts (Fig. 3b), suggesting that MgO favours secondary cracking reactions (Eq. (9)). In the case of Ni/TiO₂ (Fig. 3d), the catalyst activity dramatically decreased in 40 min on stream, with conversion being 52% after 40 min on stream and H₂ yield 32%. Moreover, the high CO yield obtained revealed that this catalyst does not enhance WGS reaction. Finally, the results for Ni/SiO₂ (Fig. 3c) show a negligible oxygenate conversion (12%) and H₂ yield (1.35%), which is related to the textural properties of the support, which limit the accessibility and diffusion of bio-oil molecules to Ni sites, thereby hindering the reforming reaction [45].

The aforementioned results are in close agreement with those by Charisiou et al. [30], who studied the influence the supports Al₂O₃, SiO₂ and ZrO₂ have on the Ni catalysts performance for glycerol steam reforming. They observed that, although the Ni/Al₂O₃ catalyst was the most active and selective at zero time on stream, this catalyst underwent a dramatic drop in activity, whereas the Ni/ZrO₂ one seems to be deactivated at a lower rate. This trend was attributed to ZrO₂ ability to first adsorb and then dissociate water, enhancing the adsorption of steam and activating the gasification of hydrocarbons, which leads to a higher resistance to deactivation. Moreover, these authors also observed the low activity but high stability of the Ni/SiO₂ catalyst. Likewise, Miyazawa et al. [68] tested Ni/Al₂O₃, Ni/ZrO₂, Ni/TiO₂, Ni/

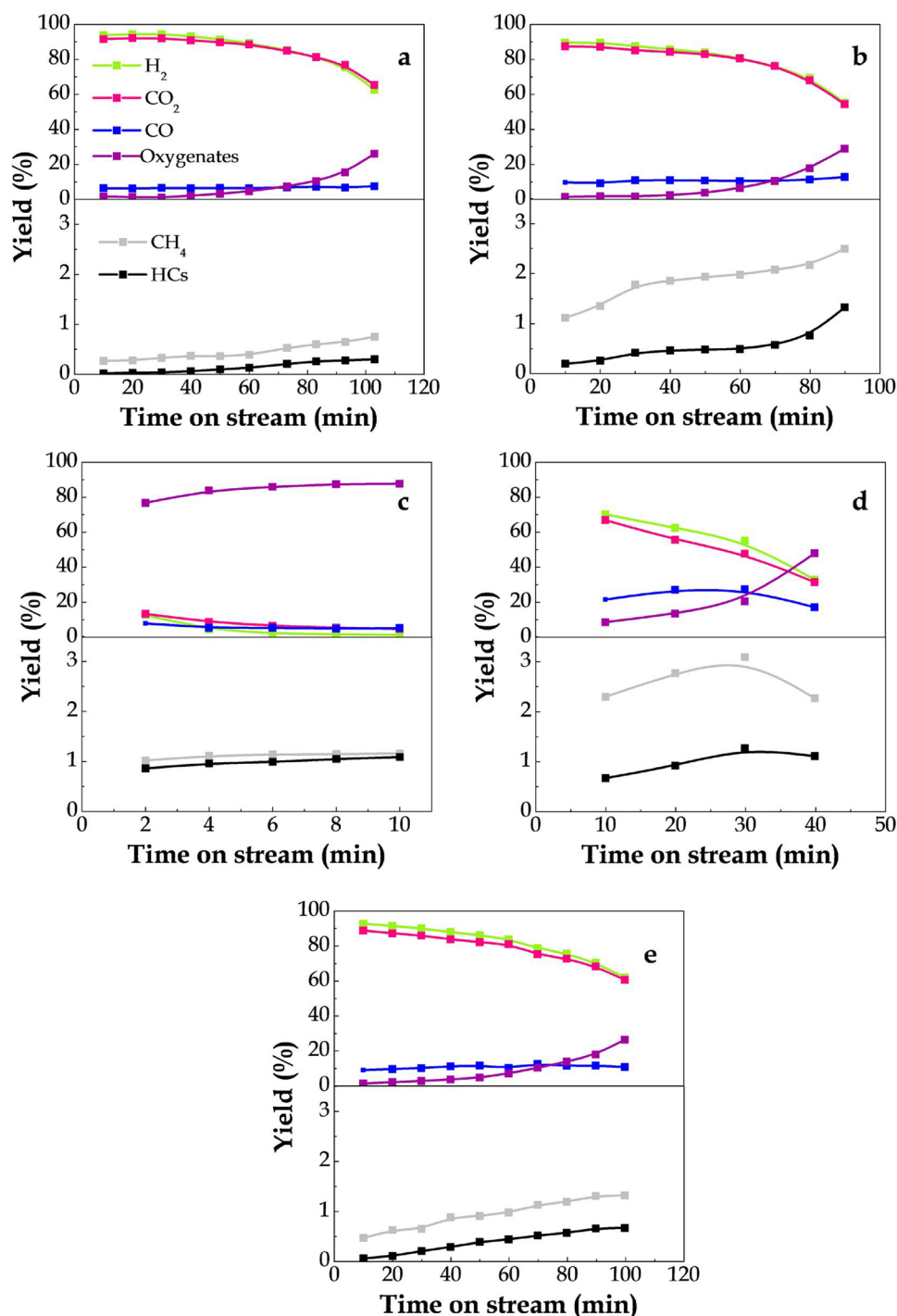


Fig. 3. Effect of the support on the evolution of the individual product yields with time on stream in the reforming step: a) Ni/Al₂O₃; b) Ni/MgO; c) Ni/SiO₂; d) Ni/TiO₂; e) Ni/ZrO₂ catalyst.

CeO₂ and Ni/MgO catalysts in the steam reforming of the tar derived from wood pyrolysis. Similarly as in this paper, Ni/Al₂O₃ and Ni/ZrO₂ showed the best performance and Ni/TiO₂ showed slightly lower activity than the others. However, they observed that MgO is not an appropriate support, since poor Ni dispersion on this support leads to lower carbon conversions.

3.3. Origin of the deactivation

The main causes of catalyst deactivation in the steam reforming of oxygenates are coke deposition and metal sintering [69], whose

influence is mainly related to the deterioration of the textural properties of the support and the properties of the supported metal, respectively. In order to ascertain whether the textural properties have undergone modifications or not during the reaction, the fresh and deactivated catalysts are compared in Table 2. As observed, the volume and diameter of the pores in Ni/Al₂O₃, Ni/TiO₂ and Ni/ZrO₂ catalysts decreased due to partial blockage of their pores by coke deposition. The specific surface area decreased slightly for the studied catalysts, since this partial blockage did not lead to a complete clogging of the catalyst pores. In the case of Ni/MgO catalyst, a more severe blockage was observed, decreasing the size of the pores from 719 to 209 Å. This

Table 2
Properties of the fresh and deactivated catalysts.

Catalyst	S_{BET}		V_p		d_p	
	$(\text{m}^2 \text{g}^{-1})$		$(\text{cm}^3 \text{g}^{-1})$		(\AA)	
	fresh	deact.	fresh	deact.	fresh	deact.
Ni/Al ₂ O ₃	76	75	0.39	0.29	182	153
Ni/MgO	6	8	0.09	0.04	719	209
Ni/SiO ₂	429	385	0.12	0.11	53	57
Ni/TiO ₂	22	21	0.22	0.13	365	271
Ni/ZrO ₂	34	30	0.31	0.21	322	281

decrease is due to the limited textural properties of the Ni/MgO catalyst. In addition, coke deposition in the catalysts supported on Al₂O₃, ZrO₂ and TiO₂ occurred in the biggest pores (they are partially blocked), thereby reducing their size. Accordingly, the specific surface area remained almost constant because the pores are not completely blocked. In the Ni/SiO₂ catalyst, the textural properties were slightly affected because the time on stream of this catalyst was short, and it therefore underwent a limited coke deposition. In fact, its porous structure does not allow the diffusion of large bio-oil molecules.

In order to evaluate the changes in the metallic structure after the reaction, the X-ray diffraction patterns of the fresh (reduced) and deactivated catalysts are shown in Figs. 4a and 4b, respectively. Diffraction lines at $2\theta = 44^\circ$, 52° and 76° are attributed to crystalline phases of Ni⁰ corresponding to planes (1 1 1), (2 0 0) and (2 2 0), respectively [70]. It is worth mentioning that the NiO crystalline phase was not detected neither in the fresh (reduced) nor in the deactivated samples of Ni/Al₂O₃, Ni/SiO₂, Ni/TiO₂ and Ni/ZrO₂ catalysts, which is evidence that a loss of active phase by oxidation of Ni⁰ sites had not occurred. In the MgO supported catalyst, a complete solid solution of NiO in MgO was observed in all the diffraction peaks due to the strong metal-support interaction.

No significant differences are observed in the spectra shown in Fig. 4 for the fresh and deactivated catalysts, with the exception of Ni/TiO₂ catalyst, in which the transformation of the anatase phase into rutile is evidenced. This phase change had already been observed in the reduction of the catalyst, when the fresh Ni/TiO₂ catalyst constituted mainly by anatase (XRD not shown) was partially transformed into rutile subsequent to its reduction. Once the reaction had been carried out (Fig. 4b), this phase change of TiO₂ anatase into TiO₂ rutile was more pronounced, and therefore this may be the reason of the low activity and stability of this catalyst. Thus, this phase transformation led to a notable reduction in the BET surface area from $154 \text{ m}^2 \text{g}^{-1}$ for the TiO₂ support to $22 \text{ m}^2 \text{g}^{-1}$ for the Ni/TiO₂ catalyst (Table 2).

Although the transformation of one crystalline phase into another is an energy intensive process, this phase change (involving 15% of the initial anatase) was observed by Raj et al. [71] after the reduction. Moreover, Nichele et al. [72] reported that, due to this phase change, the Ni/TiO₂ catalyst prepared by impregnating the non-calcined support was almost completely inactive for glycerol steam reforming.

In order to estimate the possible growth of Ni⁰ particles, and so elucidate whether sintering is a potential cause of catalyst activity decay, Ni particle size may be determined using Scherrer equation (Eq. (1)). The results in Table 3 reveal that the Ni particle size has not considerably increased under the reaction conditions, and so the sintering phenomena is not responsible for the catalyst activity decay. The estimation of Ni particle size in the Ni/MgO catalyst is not possible due to the strong interaction between the active phase and the support. These results remark the relevance of a strong metal-support interaction to avoid Ni sintering. Li et al. [37] reported that, in the case of supported Ni catalysts with weak metal-support interaction, Ni particle size is liable to grow up due to sintering (by migration and subsequent agglomeration) above the Tammann temperature of 864 K. The

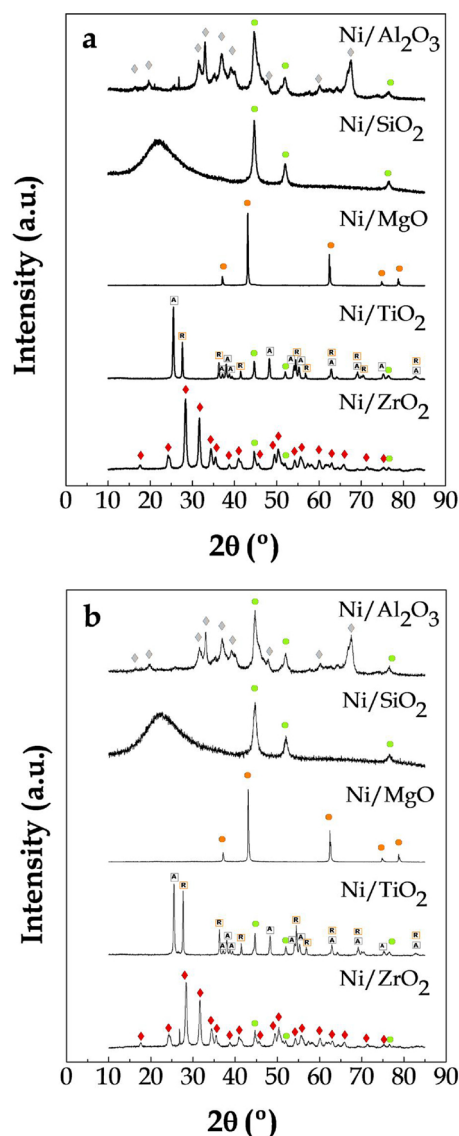


Fig. 4. XRD patterns of the fresh (reduced) (a), and deactivated catalysts (b). Crystalline phases: (●) Ni (◆) Al₂O₃ (●) NiO/MgO (□) TiO₂ (Anatase) (□) TiO₂ (Rutile) (◆) ZrO₂.

presence of strong metal-support interaction (SMSI) would prevent Ni sintering at moderate temperatures, increasing the dispersion of Ni and the extent of the interfacial boundary between Ni and the support [37].

Table 3
Values of coke content on the catalyst (C_c) and average coke deposition rate (r_c).

Catalyst	dp Ni ^a		C _c	r _c (mg _{soke} g _{cat} ⁻¹ g _{biomass} ⁻¹)
	(nm)			
	fresh	deact.		
Ni/Al ₂ O ₃	10	13	2.84	0.37
Ni/MgO	–	–	0.89	0.13
Ni/SiO ₂	11	11	0.60	0.80
Ni/TiO ₂	49	51	5.47	1.83
Ni/ZrO ₂	25	27	1.93	0.26

^a Calculated from the full width at half-maximum of the Ni (2 0 0) diffraction peak at $2\theta = 52^\circ$ in the XRD using the Scherrer equation.

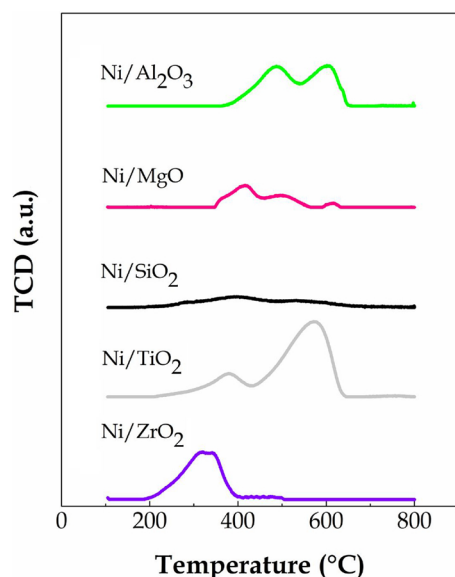


Fig. 5. TPO profiles of the deactivated catalysts. Catalysts time on stream: Ni/Al₂O₃ 103 min; Ni/MgO 90 min; Ni/SiO₂ 10 min; Ni/TiO₂ 40 min; Ni/ZrO₂ 100 min.

3.4. Coke deposition

In view of the previously mentioned results, catalyst activity evolution with time on stream is related to coke deposition, which has been analyzed by temperature programmed oxidation (TPO), as described in section 2.2. The extent of coke deposition is shown in Table 3, in which the values of coke content in the catalyst, wt%, and the average coke deposition rate per catalyst mass unit are set out. These values have been obtained from the TPO profiles (Fig. 5), and the average coke deposition rate has been assessed by considering the different times on stream for each catalyst (Figs. 2 and 3). Notable differences are observed in Table 3, with Ni/MgO and Ni/ZrO₂ being the catalysts on which the lowest amount of coke had been deposited and also those that underwent the lowest average coke deposition rate (0.13 and 0.26 mg_{coke} g_{cat}^{−1} g_{biomass}^{−1}, respectively). This is an especially relevant result, as their initial activity is lower than for the catalyst supported on Al₂O₃, and therefore it was obtained under higher oxygenate concentration throughout the reaction. According to previous literature, the lower coke formation is related to the basic properties of MgO [35,73–75] and the redox capacity and oxygen storage capacity of ZrO₂ [30,38,76]. In addition, some studies have concluded that the solid solution of NiO-MgO formed in the Ni/MgO catalyst inhibits coke deposition [35].

The values of coke content and average rate of coke deposition on the Ni/Al₂O₃ catalyst were high (2.84 wt% and 0.37 mg_{coke} g_{cat}^{−1} g_{biomass}^{−1}) and led to catalyst deactivation. Although this support has been widely used in reforming reactions due to its mechanical strength and suitable dispersion of Ni active sites, the acidic properties of alumina favour the formation of carbon deposits [30,32]. The Ni/TiO₂ catalyst showed the highest average rate of coke deposition (1.83 mg_{coke} g_{cat}^{−1} g_{biomass}^{−1}). As previously mentioned, the phase transformation of the support (anatase into rutile), both in the activation of Ni by reduction at 710 °C in a 10% H₂ stream and in the reforming step, results in bigger Ni crystal sizes and poorer Ni dispersion, which favour coke formation. Moreover, the high concentration of oxygenates (coke precursors) and acid character of titanol species also contribute to coke deposition [43]. Some authors have correlated the stability of Ni catalysts with the formation of a strong metal-support interaction, which helps in keeping dispersed the Ni particles during the reaction, thus limiting coke deposition [77]. Accordingly, thermal

stabilization improves the activity and stability of the Ni/TiO₂ catalyst. In the case of the Ni/MgO catalyst, the reduced coke formation rate observed is related to the basic properties of MgO support [35]. Similarly, the basic properties of ZrO₂ also delay coke deposition.

The different peaks observed in the TPO profiles in Fig. 5 clearly reveal the heterogeneous nature of the coke. In the literature, the combustion temperature of the coke on metal supported catalysts is associated with two essential coke features [78,79]: the location on the catalysts and its composition. Thus, a lower combustion temperature corresponds to a fraction of coke deposited on metallic sites (encapsulating coke), which catalyzes combustion, whereas a higher temperature combustion is related to the coke deposited on the support, and therefore the combustion cannot be catalytically activated by Ni sites. Moreover, at the same coke location, combustion temperature is higher as the condensation degree increases towards more ordered structures with lower H/C ratios.

The differences in the number of peaks (indicative of coke heterogeneity) and in their combustion temperature in Fig. 5 reveal great differences in the coke characteristics and the role played by the support. It is noteworthy that the initial activity and stability of Ni/Al₂O₃, Ni/MgO and Ni/ZrO₂ catalyst did not differ greatly (Fig. 2), but significant differences are observed in their TPO profiles. In the TPO of Ni/Al₂O₃ catalyst, the peaks at 490 and 580 °C are related to the combustion of the coke deposited on Ni sites and on the support, respectively. The acid sites of the Al₂O₃ may presumably promote the initial deposition of coke precursors, as well as their condensation on the support [80,81]. The combustion of the coke on Ni/MgO and Ni/ZrO₂ catalysts takes place at lower temperatures than that on the Ni/Al₂O₃ catalyst due to the basic properties of MgO and ZrO₂ supports [34–36], which delay the condensation of coke precursors. However, the TPO profiles for MgO and ZrO₂ are very different, with the coke deposited on Ni/ZrO₂ catalysts having two peaks overlapped at low temperatures (at 310 and 350 °C). This low combustion is very interesting for the use of this catalyst in reaction-regeneration cycles, and is probably a consequence of the characteristics of the ZrO₂ support, as are: i) its capacity for enhancing the adsorption of steam onto its surface and so activating the gasification of the carbon precursors adsorbed throughout the steam reforming reactions [82], which hinders the evolution of the coke into a more structured material and leads to lower carbon deposition, as observed in Table 3; ii) the well-known capacity of ZrO₂ for storing O₂ [38] favours the combustion of carbonaceous deposits at lower temperatures; iii) the higher surface area and greater pore volume of ZrO₂ compared to other supports, such as MgO (Table 2), favour O₂ diffusion into the porous structure and the contact with the deposited coke. Furthermore, the low capacity of MgO for coke gasification in the reforming is well established in the literature [35]. Moreover, the Ni/MgO catalyst is characterized by low surface area and pore volume values, which may hinder O₂ diffusion during coke combustion. The heterogeneity of the coke deposited on the Ni/MgO catalyst is consistent with the TPO results by Djaidja et al. [35] for catalysts deactivated in the dry reforming of methane. Thus, these authors observed four peaks, with the first two being associated with the hydrogenated coke, the third one with nickel carbide species and the last one with carbon nanotubes.

Ni/TiO₂ presents two different types of coke, with the peak at higher temperature (580 °C) being more prominent, which is evidence of the evolution of amorphous coke into a more condensed coke due to the characteristics of TiO₂ support (low dispersion, phase transformation, presence of titanol groups) favoring the formation of condensed coke.

In addition, in order to deepen in the study of the coke nature, a technique combining simultaneously TPO and FTIR has been fine-tuned. This strategy allows identifying different functional groups constituting the coke material, by registering the FTIR bands in the 500–4000 cm^{−1} range and their simultaneous relationship with the temperature at which the coke burns (observed by TPO). Thus, the

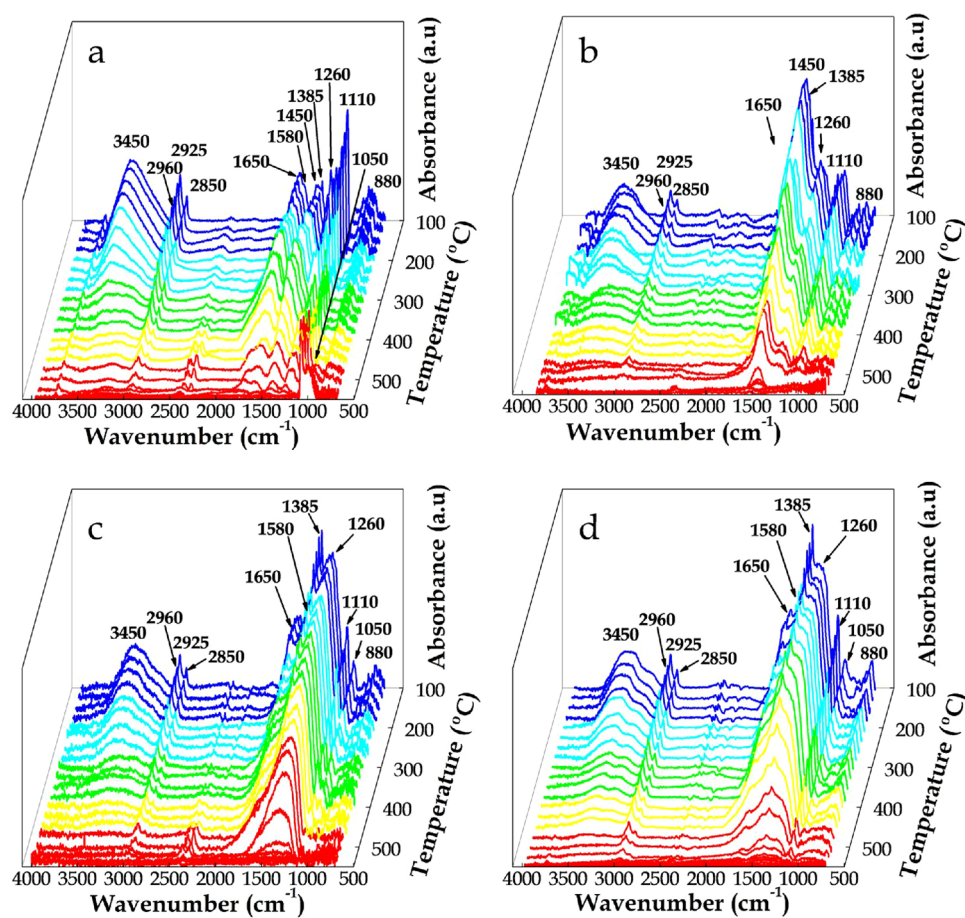


Fig. 6. Evolution of FTIR spectra under TPO conditions for the deactivated catalysts: a) Ni/Al₂O₃; b) Ni/MgO; c) Ni/TiO₂; d) Ni/ZrO₂.

Table 4

Functional groups associated with IR bands.

IR band (cm ⁻¹)	Functional group
880	–COOH deformation vibration
1050 and 1110	Stretching vibration in C–O bonds or oxides in the support
1260	Stretching vibration in C–O bonds in alcohols, ethers or related compounds, and/or stretching asymmetric vibrational mode of C–O–C bonds
1385	C–H in aliphatic compounds
1450	Bending vibrations in –CH ₂ and –CH ₃ aliphatic groups and/or symmetric stretching vibrations of O=C–O bonds in acetate groups
1505	Symmetric stretching vibrations of O=C–O bonds in carbonate groups and/or C=C in low condensed aromatic compounds
1580	C=C in polycondensed aromatic compounds or asymmetric stretching vibrations of O=C–O bonds in acetate groups
1650	C=C stretching vibrations in cyclic alkenes and/or C=O stretching vibrations in aldehydes and ketones
2850, 2925 and 2960	Stretching vibration of C–H in –CH _n aliphatic groups
3450	Stretching vibration of O–H bonds, corresponding to adsorbed water

evolution of the functional groups constituting the coke with combustion temperature has been monitored. The results corresponding to the different catalysts studied are shown in Fig. 6. It is important to note that this study has not been carried out for the Ni/SiO₂ catalyst, as it has been considered of limited relevance due to its poor performance in the reforming reaction. According to the literature, the bands observed correspond to several functional groups of the coke [81,83,84], which are summarized in Table 4. The distribution of the IR bands is complex, as they correspond to cokes with remarkable presence of oxygenated compounds, which is consistent with the coke composition reported for bio-oil steam reforming [81].

Fig. 7 shows the SEM images of the deactivated catalysts. These images complement the results obtained in the TPO analysis, and allow analyzing the morphology of the coke deposited. Thus, the presence of amorphous and disordered coke is observed in all the samples, which is more condensed on Ni supported on TiO₂. In addition, a thin layer of

coke covering the surface of Ni/Al₂O₃, Ni/MgO and Ni/ZrO₂ catalysts is observed. Moreover, no filamentous coke is observed, even though this type of coke has been registered in the reforming of bio-oil model compounds, such as ethanol [77,85], glycerol [43,86] and predominantly in the reforming of hydrocarbons [58,87–89]. The lack of filamentous coke in the biomass pyrolysis and in-line reforming was previously reported by Arregi et al. [78] and may be due to the high steam/oxygenate ratio. Thus, in the pyrolysis and catalytic steam reforming of waste biomass in a continuous screw kiln reactor, Efika et al. [17] corroborated by SEM images that the NiO/Al₂O₃ catalyst contained filamentous carbon on the surface.

TEM images (transmission electron microscopy) for all the deactivated catalysts are shown in Fig. 8, in which the morphology of the supports and of the coke deposited is observed. It should be noted that the different sizes of Ni particles (dark areas) observed in TEM images are consistent with the values calculated by XRD technique (Table 3).

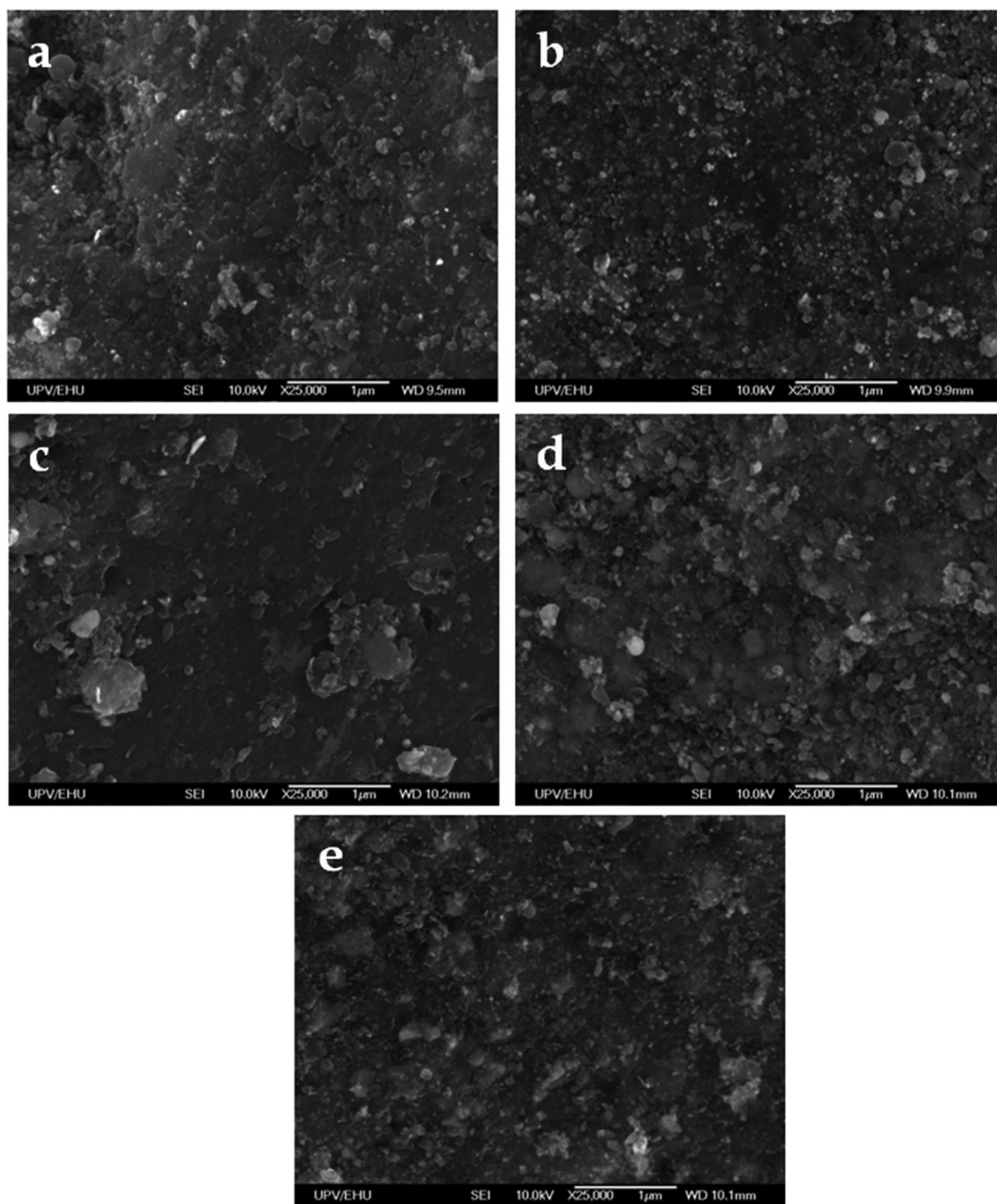


Fig. 7. SEM images of deactivated catalysts: a) Ni/Al₂O₃; b) Ni/MgO; c) Ni/SiO₂; d) Ni/TiO₂; e) Ni/ZrO₂.

Therefore, the low dispersion of Ni/TiO₂ and Ni/ZrO₂ catalysts is well proven. In these images, the coke does not show any specific morphology (amorphous coke), and filamentous coke is not observed. Thus, carbonaceous deposits make up a layer encapsulating both the catalyst surface and the Ni active sites. In the case of Ni/TiO₂ and Ni/SiO₂ catalysts, a high amount of coke appears coating mainly the support, whereas in the catalysts supported on Al₂O₃, and especially on MgO, the amorphous coke covering Ni particles can be distinguished.

4. Conclusions

The strategy of biomass pyrolysis and in-line reforming of volatiles in a system of two reactors (CSBR-FBR) has proven to be a suitable process for H₂ production from biomass. However, catalyst deactivation is fast due to the deposition of coke that blocks Ni sites, with oxygenates

being the coke precursors, as evidenced by the nature of the deposited coke.

The performance and stability of the catalysts used in the reforming of biomass pyrolysis volatiles are greatly influenced by the support. This fact is associated with the complex role of the support in the steps involving the reforming of the oxygenate compounds contained in the bio-oil and in the formation of the coke. Thus, the extent of the reactions and the significance of the deactivation are consequences of supports properties, as are: i) textural properties, as they have a great influence on Ni dispersion, accessibility of bio-oil molecules, porous structure blockage and regeneration by coke combustion; ii) chemical properties, namely, metal-support interaction (promotes the stability of the catalyst), activity for in-situ coke gasification, acidity (favors coke formation and condensation), and basicity (hinders coke formation). Although the properties of the supports used may lead to opposite

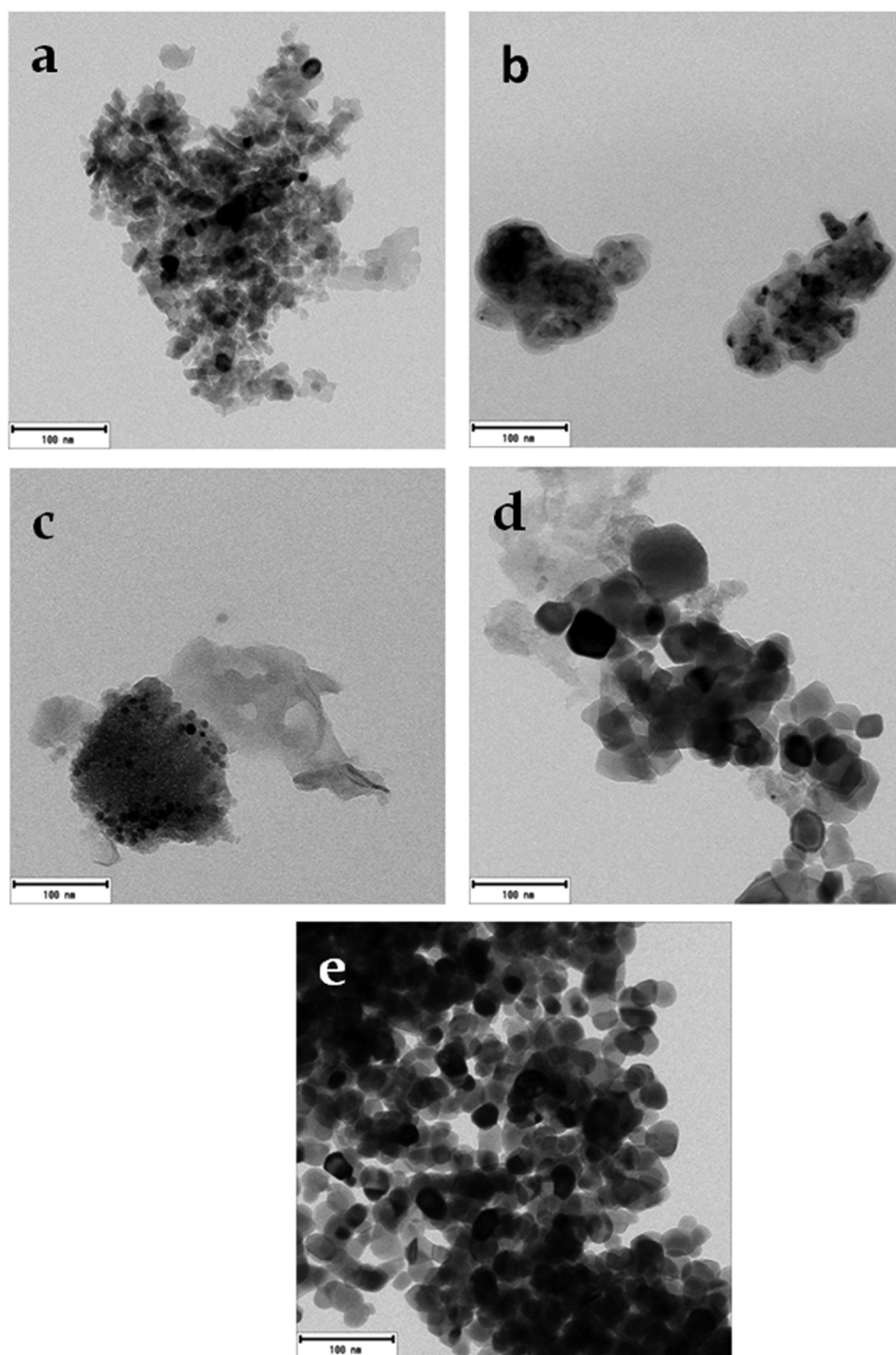


Fig. 8. TEM images of deactivated catalysts: a) Ni/Al₂O₃; b) Ni/MgO; c) Ni/SiO₂; d) Ni/TiO₂; e) Ni/ZrO₂.

effects, Ni/Al₂O₃, Ni/ZrO₂ and Ni/MgO catalysts are overall more active and stable over time on stream, without sintering being a possible cause of catalyst activity decay. Despite the high metal dispersion and initial activity of Ni/Al₂O₃ catalyst, it led to a remarkable coke deposition and a moderate deactivation rate. Furthermore, Ni/ZrO₂ and Ni/MgO catalysts are less active, but their deactivation rate is lower, i.e., lower coke contents, due to the properties conferred by ZrO₂ and MgO supports upon the catalysts, as are basicity and capacity, respectively, for gasifying the coke precursors. From the perspective of catalyst regeneration, the surface area and pore volume of the Ni/ZrO₂

catalyst is higher than those of the Ni/MgO catalyst, which allows removing the coke at lower temperatures. This result is relevant for the use of the Ni/ZrO₂ catalyst in reaction-regeneration cycles.

The instability of the Ni/TiO₂ catalyst is attributed to the phase transformation of the support (anatase into rutile) both in the activation step and in the reforming process, entailing a decrease in the dispersion values, and therefore leading to a poorer reforming activity and enhancing coke deposition. The low activity of the Ni/SiO₂ catalyst is due to the microporous structure of the SiO₂, limiting the accessibility and diffusion of oxygenates derived from the pyrolysis into the Ni active sites.

Acknowledgments

This work was carried out with financial support from the Ministry of Economy and Competitiveness of the Spanish Government (CTQ2016-75535-R (AEI/FEDER, UE) and CTQ2015-69436-R (MINECO/FEDER, UE)) and the Basque Government (IT748-13). Aitor Arregi thanks the University of the Basque Country for his postgraduate grant (UPV/EHU 2017).

References

- [1] H. Balat, E. Kirtay, *Int. J. Hydrogen Energy* 35 (2010) 7416–7426.
- [2] N.L. Panwar, R. Kothari, V.V. Tyagi, *Renew. Sustain. Energy Rev.* 16 (2012) 1801–1816.
- [3] G. Guan, G. Chen, Y. Kasai, E. Lim Wee Chuan, X. Hao, M. Kaewpanha, A. Abuliti, C. Fushimi, A. Tsutsumi, *Appl. Catal. B* 115–116 (2012) 159–168.
- [4] A. Arregi, M. Amutio, G. Lopez, J. Bilbao, M. Olazar, *Energy Convers. Manage.* 165 (2018) 696–719.
- [5] R. Parajuli, T. Dalgaard, U. Jørgensen, A.P.S. Adamsen, M.T. Knudsen, M. Birkved, M. Gylling, J.K. Schjørring, *Renew. Sustain. Energy Rev.* 43 (2015) 244–263.
- [6] G. Guan, M. Kaewpanha, X. Hao, A. Abudula, *Renew. Sustain. Energy Rev.* 58 (2016) 450–461.
- [7] M.M. Yung, W.S. Jablonski, K.A. Magrini-Bair, *Energy Fuels* 23 (2009) 1874–1887.
- [8] A. Erkiaga, G. Lopez, M. Amutio, J. Bilbao, M. Olazar, *Fuel Process Technol.* 116 (2013) 292–299.
- [9] A. Nzihou, B. Stanmore, P. Sharrock, *Energy* 58 (2013) 305–317.
- [10] P.J. Woolcock, R.C. Brown, *Biomass Bioenergy* 52 (2013) 54–84.
- [11] P. Knutsson, V. Cantatore, M. Seemann, P.L. Tam, I. Panas, *Appl. Catal. B* 229 (2018) 88–95.
- [12] P.H. Moud, K.J. Andersson, R. Lanza, K. Engvall, *Appl. Catal. B* 190 (2016) 137–146.
- [13] S. Czernik, R. French, *Int. J. Hydrogen Energy* 39 (2014) 744–750.
- [14] R. Trane, S. Dahl, M.S. Skjoth-Rasmussen, A.D. Jensen, *Int. J. Hydrogen Energy* 37 (2012) 6447–6472.
- [15] A.C. Basagiannis, X.E. Verykios, *Catal. Today* 127 (2007) 256–264.
- [16] J. Alvarez, S. Kumagai, C. Wu, T. Yoshioka, J. Bilbao, M. Olazar, *Int. J. Hydrogen Energy* 39 (2014) 10883–10891.
- [17] C.E. Erika, C. Wu, P.T. Williams, *J. Anal. Appl. Pyrolysis* 95 (2012) 87–94.
- [18] M. Koike, C. Ishikawa, D. Li, L. Wang, Y. Nakagawa, K. Tomishige, *Fuel* 103 (2013) 122–129.
- [19] A. Arregi, G. Lopez, M. Amutio, I. Barbarias, J. Bilbao, M. Olazar, *RSC Adv.* 6 (2016) 25975–25985.
- [20] G. Lopez, M. Artetxe, M. Amutio, J. Alvarez, J. Bilbao, M. Olazar, *Renew. Sustain. Energy Rev.* 82 (2018) 576–596.
- [21] D. Yao, H. Yang, H. Chen, P.T. Williams, *Appl. Catal. B* 227 (2018) 477–487.
- [22] B. Valle, A. Remiro, A.T. Aguayo, J. Bilbao, A.G. Gayubo, *Int. J. Hydrogen Energy* 38 (2013) 1307–1318.
- [23] R. Trane-Restrup, A.D. Jensen, *Appl. Catal. B* 165 (2015) 117.
- [24] C.H. Bartholomew, *Appl. Catal. A Gen.* 212 (2001) 17–60.
- [25] A.A. Lemonidou, P. Kechagiopoulos, E. Heracleous, S. Voutetakis, *The Role of Catal. for the Sustain. Prod. of Bio-Fuels and Bio-Chem.* (2013) 467–493.
- [26] L. Wang, D. Li, M. Koike, S. Koso, Y. Nakagawa, Y. Xu, K. Tomishige, *Appl. Catal. A Gen.* 392 (2011) 248–255.
- [27] R. Xing, V.L. Dagle, M. Flake, L. Kovarik, K.O. Albrecht, C. Deshmane, R.A. Dagle, *Catal. Today* 269 (2016) 166.
- [28] F. Auprêtre, C. Descorme, D. Duprez, *Catal. Commun.* 3 (2002) 263–267.
- [29] D. Li, M. Tamura, Y. Nakagawa, K. Tomishige, *Bioresour. Technol.* 178 (2015) 53–64.
- [30] N.D. Charisiou, K.N. Papageridis, G. Siakavelas, L. Tzounis, K. Kousi, M.A. Baker, S.J. Hinder, V. Sebastian, K. Polychronopoulou, M.A. Goula, *Top. Catal.* 60 (2017) 1226–1250.
- [31] N.D. Charisiou, G. Siakavelas, K.N. Papageridis, A. Baklavaridis, L. Tzounis, D.G. Avraam, M.A. Goula, *J. Nat. Gas Sci. Eng.* 31 (2016) 164–183.
- [32] M.C. Sánchez-Sánchez, R.M. Navarro, J.L.G. Fierro, *Int. J. Hydrogen Energy* 32 (2007) 1462–1471.
- [33] F. Huang, R. Wang, C. Yang, H. Driss, W. Chu, H. Zhang, *J. Energy Chem.* 25 (2016) 709–719.
- [34] A. Kambolis, H. Matralis, A. Trovarelli, C. Papadopoulou, *Appl. Catal. A Gen.* 377 (2010) 16–26.
- [35] A. Djajidja, S. Libs, A. Kiennemann, A. Barama, *Catal. Today* 113 (2006) 194–200.
- [36] S. Adhikari, S.D. Fernando, A. Haryanto, *Renew. Energy* 33 (2008) 1097–1100.
- [37] S. Li, M. Li, C. Zhang, S. Wang, X. Ma, J. Gong, *Int. J. Hydrogen Energy* 37 (2012) 2940–2949.
- [38] F. Pompeo, N.N. Nichio, M.M.V.M. Souza, D.V. Cesar, O.A. Ferretti, M. Schmal, *Appl. Catal. A Gen.* 316 (2007) 175–183.
- [39] T. Yamaguchi, *Catal. Today* 20 (1994) 199–217.
- [40] J.G. Seo, M.H. Youn, S. Park, J. Lee, S.H. Lee, H. Lee, I.K. Song, *Korean J. Chem. Eng.* 25 (2008) 95–98.
- [41] Y. Matsumura, T. Nakamori, *Appl. Catal. A Gen.* 258 (2004) 107–114.
- [42] B. Matas Güell, I.M.Td. Silva, K. Seshan, L. Lefferts, *Appl. Catal. B* 88 (2009) 59–65.
- [43] I. Rossetti, A. Gallo, V. DalSanto, C.L. Bianchi, V. Nichele, M. Signoretto, E. Finocchio, G. Ramis, A. Di Michele, *ChemCatChem* 5 (2013) 294–306.
- [44] E.T. Kho, J. Scott, R. Amal, *Chem. Eng. Sci.* 140 (2016) 161–170.
- [45] L. Santamaria, G. Lopez, A. Arregi, M. Amutio, M. Artetxe, J. Bilbao, M. Olazar, *Appl. Catal. B* 229 (2018) 105–113.
- [46] A. Arregi, M. Amutio, G. Lopez, M. Artetxe, J. Alvarez, J. Bilbao, M. Olazar, *Energy Convers. Manage.* 136 (2017) 192–201.
- [47] L. An, C. Dong, Y. Yang, J. Zhang, L. He, *Renew. Energy* 36 (2011) 930–935.
- [48] Z. Zhang, X. Hu, J. Li, G. Gao, D. Dong, R. Westerhof, S. Hu, J. Xiang, Y. Wang, *Fuel* 217 (2018) 389–403.
- [49] I. Barbarias, G. Lopez, J. Alvarez, M. Artetxe, A. Arregi, J. Bilbao, M. Olazar, *Chem. Eng. J.* 296 (2016) 191–198.
- [50] M. Amutio, G. Lopez, M. Artetxe, G. Elordi, M. Olazar, J. Bilbao, *Resour. Conserv. Recycl.* 59 (2012) 23–31.
- [51] J. Alvarez, M. Amutio, G. Lopez, I. Barbarias, J. Bilbao, M. Olazar, *Chem. Eng. J.* 273 (2015) 173–183.
- [52] M. Artetxe, G. Lopez, M. Amutio, G. Elordi, J. Bilbao, M. Olazar, *Ind. Eng. Chem. Res.* 52 (2013) 10637–10645.
- [53] M. Artetxe, G. Lopez, M. Amutio, I. Barbarias, A. Arregi, R. Aguado, J. Bilbao, M. Olazar, *Waste Manage.* 46 (2015) 126–133.
- [54] G. Lopez, M. Olazar, R. Aguado, J. Bilbao, *Fuel* 89 (2010) 1946–1952.
- [55] G. Lopez, J. Alvarez, M. Amutio, N.M. Mkhize, B. Danon, P. van der Grypt, J.F. Görgens, J. Bilbao, M. Olazar, *Energy Convers. Manage.* 142 (2017) 523–532.
- [56] S. Zhang, X. Li, Q. Li, Q. Xu, Y. Yan, *J. Anal. Appl. Pyrolysis* 92 (2011) 158–163.
- [57] A. Remiro, B. Valle, A.T. Aguayo, J. Bilbao, A.G. Gayubo, *Fuel Process. Technol.* 115 (2013) 222–232.
- [58] I. Barbarias, G. Lopez, M. Artetxe, A. Arregi, L. Santamaria, J. Bilbao, M. Olazar, *J. Anal. Appl. Pyrolysis* 122 (2016) 502–510.
- [59] J. Moulijn, A. Van Diepen, F. Kapteijn, *Handbook of Heterogeneous Catalysis*, (2010), pp. 1–17.
- [60] J.A. Garcia-Nunez, M.R. Pelaez-Samaniego, M.E. Garcia-Perez, I. Fonts, J. Abrego, R.J.M. Westerhof, M. Garcia-Perez, *Energy Fuels* 31 (2017) 5751–5775.
- [61] G. Lopez, M. Artetxe, M. Amutio, J. Bilbao, M. Olazar, *Renew. Sustain. Energy Rev.* 73 (2017) 346–368.
- [62] G. Perkins, T. Bhaskar, M. Konarova, *Renew. Sustain. Energy Rev.* 90 (2018) 292–315.
- [63] A.V. Bridgwater, *Biomass Bioenergy* 38 (2012) 68–94.
- [64] J. Alvarez, G. Lopez, M. Amutio, J. Bilbao, M. Olazar, *Bioresour. Technol.* 170 (2014) 132–137.
- [65] A.C. Basagiannis, X.E. Verykios, *Catal. Today* 127 (2007) 256.
- [66] Q.M.K. Waheed, C. Wu, P.T. Williams, *J. Energy Inst.* 89 (2016) 657–667.
- [67] M. Ye, Y. Tao, F. Jin, H. Ling, C. Wu, P.T. Williams, *J. Huang, Catal. Today* 307 (2018) 154–161.
- [68] T. Miyazawa, T. Kimura, J. Nishikawa, S. Kado, K. Kunitomi, K. Tomishige, *Catal. Today* 115 (2006) 254–262.
- [69] M.D. Argyle, C.H. Bartholomew, *Catalysts* 5 (2015) 145–269.
- [70] International Centre for Diffraction Data, 2003.
- [71] K.J.A. Raj, M.G. Prakash, R. Mahalakshmy, T. Elangovan, B. Viswanathan, *Catal. Sci. Technol.* 2 (2012) 1429–1436.
- [72] V. Nichele, M. Signoretto, F. Menegazzo, A. Gallo, V. Dal Santo, G. Cruciani, G. Cerrato, *Appl. Catal. B Environ.* 111–112 (2012) 225–232.
- [73] M.H. Youn, J.G. Seo, H. Lee, Y. Bang, J.S. Chung, I.K. Song, *Appl. Catal. B* 98 (2010) 57–64.
- [74] K. Sato, F. Sago, K. Nagaoka, Y. Takita, *Int. J. Hydrogen Energy* 35 (2010) 5393–5399.
- [75] M. Kong, Q. Yang, W. Lu, Z. Fan, J. Fei, X. Zheng, T.D. Wheelock, *Chinese J. Catal.* 33 (2012) 1508–1516.
- [76] N. Srisiriwat, S. Therdthianwong, A. Therdthianwong, *Int. J. Hydrogen Energy* 34 (2009) 2224–2234.
- [77] I. Rossetti, J. Lasso, E. Finocchio, G. Ramis, V. Nichele, M. Signoretto, A. Di Michele, *Appl. Catal. A Gen.* 477 (2014) 42–53.
- [78] A. Arregi, G. Lopez, M. Amutio, M. Artetxe, I. Barbarias, J. Bilbao, M. Olazar, *Fuel* 216 (2018) 233–244.
- [79] A. Ochoa, B. Valle, D.E. Resasco, J. Bilbao, A.G. Gayubo, P. Castaño, *ChemCatChem* 10 (2018) 2311–2321.
- [80] C. Montero, A. Ochoa, P. Castaño, J. Bilbao, A.G. Gayubo, *J. Catal.* 331 (2015) 181–192.
- [81] A. Ochoa, B. Aramburu, B. Valle, D.E. Resasco, J. Bilbao, A.G. Gayubo, P. Castaño, *Green Chem.* 19 (2017) 4315–4333.
- [82] J.G. Seo, M.H. Youn, I.K. Song, *J. Mol. Catal. A Chem.* 268 (2007) 9–14.
- [83] E. Pretsch, P. Bühlmann, M. Badertscher, Anonymous, *Structure Determination of Organic Compounds: Tables of Spectral Data*, (2009), pp. 1–433.
- [84] W. Xu, Z. Liu, A.C. Johnston-Peck, S.D. Senanayake, G. Zhou, D. Stacchiola, E.A. Stach, J.A. Rodriguez, *ACS Catal.* 3 (2013) 975–984.
- [85] J. Vicente, C. Montero, J. Ereña, M.J. Azkoiti, J. Bilbao, A.G. Gayubo, *Int. J. Hydrogen Energy* 39 (2014) 12586–12596.
- [86] K.N. Papageridis, G. Siakavelas, N.D. Charisiou, D.G. Avraam, L. Tzounis, K. Kousi, M.A. Goula, *Fuel Process. Technol.* 152 (2016) 156–175.
- [87] A. Ochoa, I. Barbarias, M. Artetxe, A.G. Gayubo, M. Olazar, J. Bilbao, P. Castaño, *Appl. Catal. B* 209 (2017) 554–565.
- [88] I. Barbarias, G. Lopez, M. Amutio, M. Artetxe, J. Alvarez, A. Arregi, J. Bilbao, M. Olazar, *Appl. Catal. A Gen.* 527 (2016) 152–160.
- [89] J.C. Acomb, C. Wu, P.T. Williams, *Appl. Catal. B* 147 (2014) 571–584.